Evaluation of an image-based algorithm for quantitative spectral CT applications

Björn J. Heismann[a,b] and Michael Balda[b]

[a]Siemens Healthcare, Erlangen, Germany;
[b]Friedrich-Alexander-University, Erlangen, Germany

ABSTRACT

In this paper we describe and evaluate an image-based spectral CT method. Its central formula expresses measured CT data as a spectral integration of the spectral attenuation coefficient multiplied by a Local Weighting Function (LWF). The LWF represents the local energy weighting in the image domain, taking into account the system and reconstruction properties and the object self attenuation. A generalized image-based formulation of spectral CT algorithms is obtained, with no need for additional corrections of e.g. beam hardening. The iterative procedure called Local Spectral Reconstruction (LSR) yields both the mass attenuation coefficients of the object and a representation of the LWF. The quantitative accuracy and precision of the method is investigated in several applications, including beam hardening correction, attenuation correction for SPECT/CT and PET/CT and a direct identification of spectral attenuation functions using the LWF result is demonstrated. In all applications the ground truth of the objects is reproduced with a quantitative accuracy in the sub-percent to two percent range. An exponential convergence behavior of the iterative procedure is observed, with one to two iteration steps as a good compromise between quantitative accuracy and precision. We conclude that the method can be used to perform image-based spectral CT reconstructions with quantitative accuracy. Existing algorithms benefit from the intrinsic treatment of beam hardening and system properties. Novel algorithms are enabled to directly compare material model functions to spectral measurement data.

1. INTRODUCTION

Image-based spectral CT algorithms are used for an increasing number of research and clinical CT applications. In this paper we present the main results of the Local Spectral Reconstruction (LSR) algorithm.[1] It provides an image-based and quantitive formulation of spectral CT reconstruction tasks, including the calculation of energy calibrations, beam-hardening corrections, attenuation maps for PET and SPECT and quantitative material decompositions.

2. THEORY

2.1 Local Weighting Function

The Local Weighting Function (LWF) represents the link between the reconstructed weighted attuentuation coefficient $\bar{\mu}(\mathbf{r})$ and the spectral attenuation coefficient $\mu(E,\mathbf{r})$:

$$\bar{\mu}(\mathbf{r}) = \int_0^\infty \Omega(E,\mathbf{r})\mu(E,\mathbf{r})\mathrm{d}E \tag{1}$$

where E denotes energy and $\mathbf{r}$ is a 2-D or 3-D voxel coordinate.

The LWF model fully covers the CT measurement properties as it incorporates object self-attenuation, the X-ray source spectrum, the energy weighting of the detector and the reconstruction process. For parallel ray geometry with gantry rotation angle θ and detector coordinate t, $\Omega(E,\mathbf{r})$ can be derived as follows:

With a given system system weighting function $w(E) = \frac{S(E)D(E)}{\int_0^\infty S(E')D(E')dE'}$ for the tube spectrum $S(E)$ and the detector responsivity $D(E)$ (see Fig. 1) we define the measurement operator $\mathcal{P}\{\cdot\}$ that incorporates forward projection and attenuation value calculation:

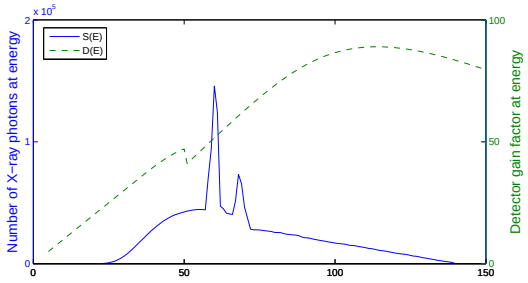

Figure 1. Typical tube spectrum $S(E)$ for a tube acceleration voltage of 140 kV and the detector responsivity $D(E)$.

$$\mathcal{P}\left\{\mu(E,\mathbf{r})\right\} = -\ln\left(\int_0^\infty w(E)\exp\left(-M_{\theta,t}(E)\right)\mathrm{d}E\right) \tag{2}$$

$M_{\theta,t}(E)$ is the path integration of the sprectral attenuation coefficients along the parameterized line $l_{\theta,t}$:

$$M_{\theta,t}(E) = \int_{-\infty}^{\infty} \mu(E, l_{\theta,t}(\alpha))\mathrm{d}\alpha. \tag{3}$$

Inverse Radon transform $\mathcal{R}^{-1}\{\cdot\}$ yields the weighted attenuation values:

$$\bar{\mu}(\mathbf{r}) = \mathcal{R}^{-1}\left\{\mathcal{P}\left\{\mu(E,\mathbf{r})\right\}\right\} \tag{4}$$

Expanding with $\frac{\mu(E,\mathbf{r})}{\mu(E,\mathbf{r})}$ and inserting $\int_0^\infty w(E)dE = 1$ leads to:

$$\bar{\mu}(\mathbf{r}) = \int_0^\infty w(E)\frac{\mathcal{R}^{-1}\left\{\mathcal{P}\left\{\mu(E,\mathbf{r})\right\}\right\}}{\mu(E,\mathbf{r})}\mu(E,\mathbf{r})\mathrm{d}E. \tag{5}$$

With (1) we get

$$\Omega(E,\mathbf{r}) = w(E)\frac{\mathcal{R}^{-1}\left\{\mathcal{P}\left\{\mu(E,\mathbf{r})\right\}\right\}}{\mu(E,\mathbf{r})}. \tag{6}$$

2.2 Calculation of the LWF

The above calculation of $\Omega(E,\mathbf{r})$ needs an approximation for $\mu(E,\mathbf{r})$. With an estimate of $\Omega(E,\mathbf{r})$ we compute $\Omega(E,\mathbf{r})$ from a dual-energy data set $\bar{\mu}_1(\mathbf{r}), \bar{\mu}_2(\mathbf{r})$ of weighted attenuation values using image-based basis material decomposition $\mathcal{B}\{\cdot\}$:[2]

$$\mu(E,\mathbf{r}) = \mathcal{B}\left\{\bar{\mu}_1(\mathbf{r}), \Omega_1(E,\mathbf{r}), \bar{\mu}_2(\mathbf{r}), \Omega_2(E,\mathbf{r})\right\} \tag{7}$$

This leads to a two-phase iteration scheme with the iteration counter i:

- Initialize: $\Omega_1^{(0)}(E,\mathbf{r}) = w_1(E)$ and $\Omega_2^{(0)}(E,\mathbf{r}) = w_2(E)$
- $\mu^{(i)}(E,\mathbf{r}) = \mathcal{B}\left\{\bar{\mu}_1(\mathbf{r}), \Omega_1^{(i-1)}(E,\mathbf{r}), \bar{\mu}_2(\mathbf{r}), \Omega_2^{(i-1)}(E,\mathbf{r})\right\}$
- $\Omega_j^{(i)}(E,\mathbf{r}) = w_1(E)\frac{\mathcal{R}^{-1}\left\{\mathcal{P}\left\{\mu^{(i)}(E,\mathbf{r})\right\}\right\}}{\mu^{(i)}(E,\mathbf{r})}$ for $j \in \{1,2\}$

The signal flow of this algorithm is depicted in Fig. 2.

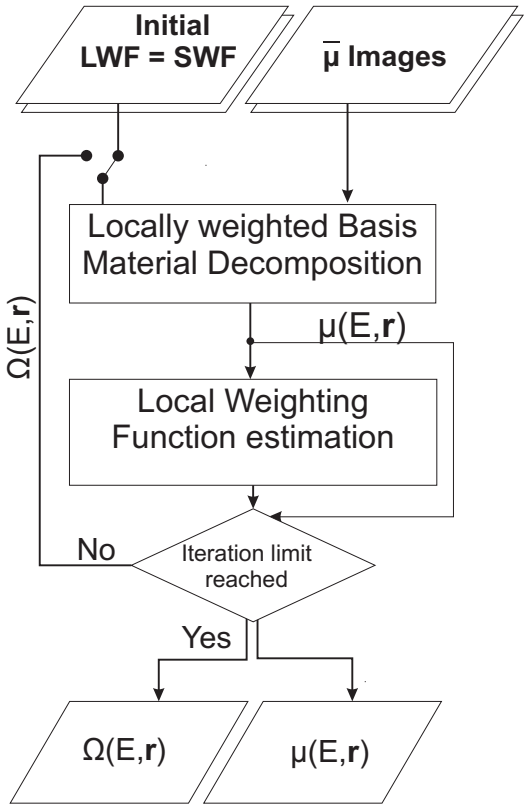

Figure 2. Flowchart of the LSR algorithm.

2.3 Applications

The LSR framework (1), (6) yields an estimate of the LWF and the object ground truth $\mu(E, \mathbf{r})$. For practical quantitative spectral CT applications, three main fields exist:

The first group of applications targets the obtained $\mu(E, \mathbf{r})$ object data. The resulting parameters like basis material coefficients can be displayed and analyzed for specific diagnostic tasks. In comparison to existing image-based calculations, the effects of beam-hardening and system energy weighting properties are incorporated quantitatively into the algorithm. We investigate the quantitative accuracy and precision in the experimental section.

It is important to note that the $\mu(E, \mathbf{r})$ are theoretically independent of object self-attenuation effects and characteristics of the reconstruction and measurement process. For example, the difference in reconstruction kernels between the two Dual-kVp measurements can be incorporated into the measurement model of Eq. (4). This can improve pixel registration between the input data sets. Note that the spatial resolution of the $\mu(E, \mathbf{r})$-estimate, however, is limited by the input image discretization.

In practice, accurate descriptions of $w(E)$ and the measurement operator $\mathcal{P}\{\cdot\}$ are required to ensure quantitative results. Note that the inverse Radon transform operator $\mathcal{R}^{-1}\{\cdot\}$ enters both the input image reconstruction and the LWF calculation in the same way. Due to this it has no additional effect on the accuracy and precision of $\mu(E, \mathbf{r})$.

Scatter radiation can be included in the measurement model, Eq. (2), or corrected by an appropriate scatter correction algorithm. For the Dual-kVp experiments carried out in this paper, scattered radiation plays only a minor role and is not corrected for.

It should be noted that alternative $\mu(E, \mathbf{r})$ parameterizations can be employed in the LSR framework. An example is the image-based RhoZ projection method.[3] Here the attenuation coefficient is modeled as

$$\mu(E, \mathbf{r}) = \rho_{\text{eff}}(\mathbf{r}) \left(\frac{\mu}{\rho}\right)(E, Z_{\text{eff}}(\mathbf{r}))\,. \tag{8}$$

In this case we obtain effective density and atomic number representations (ρ_{eff}, Z_{eff}) as a result of the LSR framework.

A second class of applications is energy calibration. Here new images are calculated which, for instance, contain the contrasts of an alternative tube voltage setting. Mathematically, this corresponds to a pre-defined, constant energy weighting $w_c(E)$ throughout the whole CT image data. A number of different target weightings exist: CT beam hardening corrections, for example, typically aim at a constant System Weighting Function throughout the image, see e.g. Fig. 3 for the $w(E)$ of CT measurements with 80 kV and 140 kV tube voltage settings.

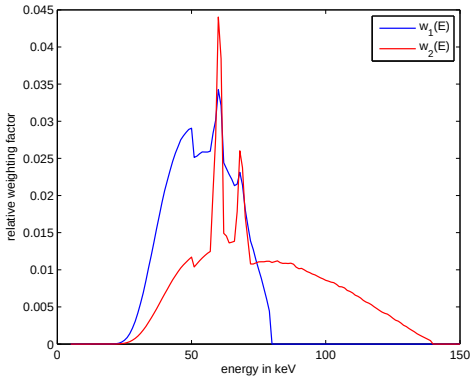

Figure 3. System Weighting Functions $w_1(E)$, $w_2(E)$ two tube spectra at 80 kVp and 140 kVp and the detector responsivity $D(E)$ in Fig. 1. The two weighting functions reflect a common dual-energy measurement case, often referred to as a Dual-kVp CT measurement.

This can be extended to mono-energetic calibrations with the target weighting function given by $w_c(E) = \delta(E - E_0)$. An application of mono-energetic attenuation coefficients is contrast enhancement for specific tissue differences.

A further energy calibration application is the attenuation correction in SPECT/CT and PET/CT. Mono-energetic attenuation coefficients at e.g. 141 keV and 511 keV for the respective tracer emission lines of ^{99m}Tc and ^{18}F-glucose are required.[4]

We can express all of the above energy calibration applications in a common formula:

$$\bar{\mu}_c(\mathbf{r}) = \int_0^\infty w_c(E)\mu(E, \mathbf{r})\, dE. \tag{9}$$

Here $\bar{\mu}_c(\mathbf{r})$ are the corrected image data for the LSR-determined $\mu(E, \mathbf{r})$ and a chosen target energy weighting $w_c(E)$.

The third field of applications employs the LWF result. Fundamentally, the LWF offers a deeper understanding of the energy weighting process in CT. In practice it allows for a direct identification of an arbitrary object material. Based on the LWF and Eq. (1), the measured spectral data $\bar{\mu}_i(\mathbf{r})$ can be compared against reference spectral attenuation functions.

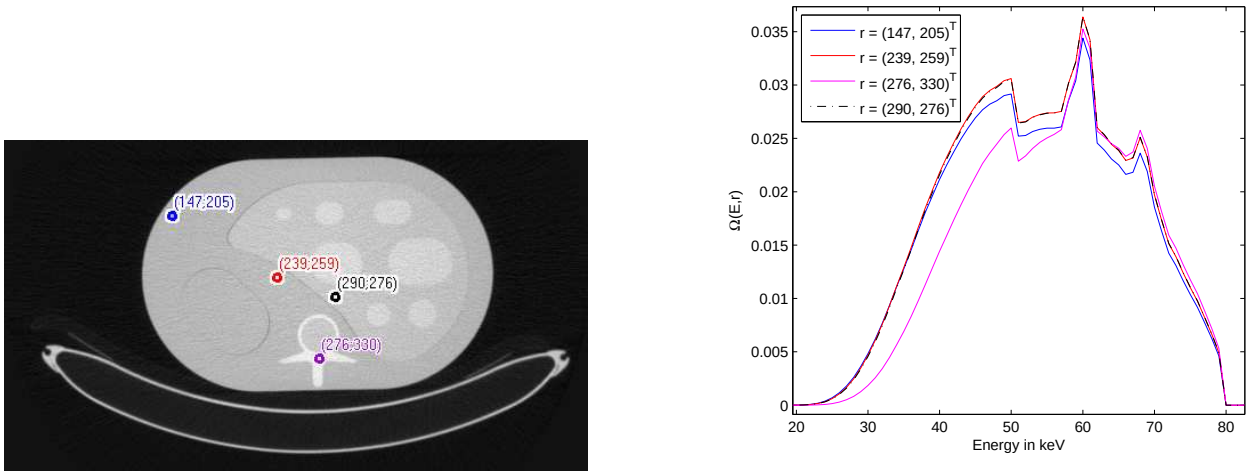

(a) (b)

Figure 4. (a) shows a CT image of the upper abdomen phantom and locations of sample points for the LWF plots of Fig. (b).

2.4 Evaluation

We evaluated the LSR method for the applications mentioned in Sec. 2.3 using simulated and measured data. For the first example the $\Omega(E, \mathbf{r})$ was estimated with the LSR iteration introduced above. Figure 4 shows the results for several materials within a liver phantom. It was scanned at 80 kVp and 140 kVp with a Siemens Definition AS+ CT scanner (Siemens Healthcare, Forchheim, Germany).

This evaluation reveals two properties of the Local Weighting Function: The shape of the LWF depends strongly on the material at the corresponding locations. For materials with higher effective atomic number like bone, the local weighting is shifted towards higher energies. This effect can be observed by comparing the soft-tissue weightings with the bone weighting (purple curve). The beam hardening is reflected by the integral value: The blue and the red curve correspond to the same soft tissue. Both curves have approximately the same shape but are scaled differently. Here, the wedge / bowtie filter of the CT device causes a stronger beam hardening than the object itself, consequently the outer blue point is affected by stronger beam hardening and its attenuation value is lower that the one at the red point.

The second example uses simulated data of a typical thorax phantom (see Fig. 6a). The phantom materials were modeled using the tissue compositions from the ICRU 46 report.[5] Here we assess precision, accuracy and convergence by comparing the LSR results with ground truth data. This is done by perfoming an energy calibration on the estimated spectral attenuation values with different target spectra $w_j(E)$:

$$\bar{\mu}_j(\mathbf{r}) = \int_0^{+\infty} w_j(E)\mu^{(i)}(E, \mathbf{r})dE \tag{10}$$

The special case where $w_j(E)$ corresponds to the original effective energy weighting of the measurement can be interpreted as quantitative beam hardening correction.

The results are compared for different phantom materials and iterations in terms of mean absolute deviation from the ground truth and the standard deviation of all voxel representing the same materials. Figure 5a shows the convergence for the average soft tissue component of the phantom for the 80 kVp beam hardening case. A fast convergence at a high accuracy can be observed: The mean absolute deviation is almost zero after only two iterations. Further iterations do not increase the accuracy. However, the standard deviation over all average soft-tissue voxels increases after the second iteration. This is due to the noise amplification of the BMD. In order to preserve the highest possible precision, the iteration should be terminated after the desired accuracy has

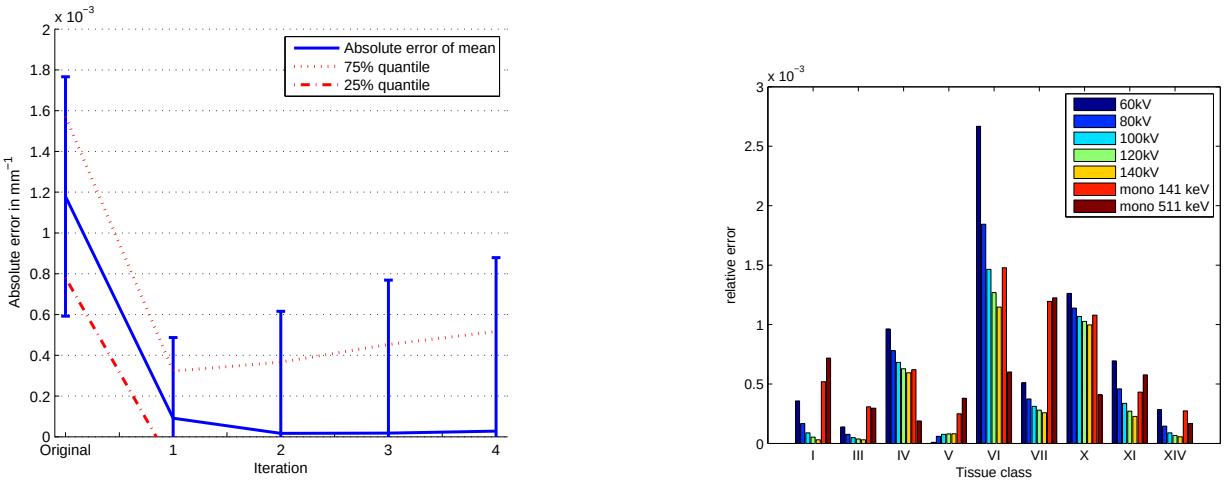

(a) (b)

Figure 5. (a) Absolute error for average soft tissue attenuation values after energy calibration with 80 kV target weighting. (b) Relative errors for energy calibration of 80 kV input data to target spectra from 60 kV to 140 kV and two mono-energetic spectra at 141 keV and 511 keV.

been reached. This evaluation has been extended to all materials of the thorax phanton and several additional target spectra including two monoenergetic ones that can be used for PET or SPECT attenuation correction. In all cases the above mentioned properties are maintained. Figure 5b shows the accuracy results after the fourth iteration.

The third evaluation is performed on the same thorax phantom. It shows a proof-of-concept for an application called material identification. A target material spectral attuenation function for an arbitrary material is given. This material can be identified by directly comparing the locally weighted spectral attuenation function with the measured Dual Energy data $\bar{\mu}_1(\mathbf{r})$ and $\bar{\mu}_2(\mathbf{r})$. Figure 6 shows an original $\bar{\mu}_1(\mathbf{r})$ image of the thorax phantom and the color-coded identification result for all soft tissues. Despite the visibly strong beam hardening and similarity of several materials such as liver and blood a good separation of all materials can be observed.

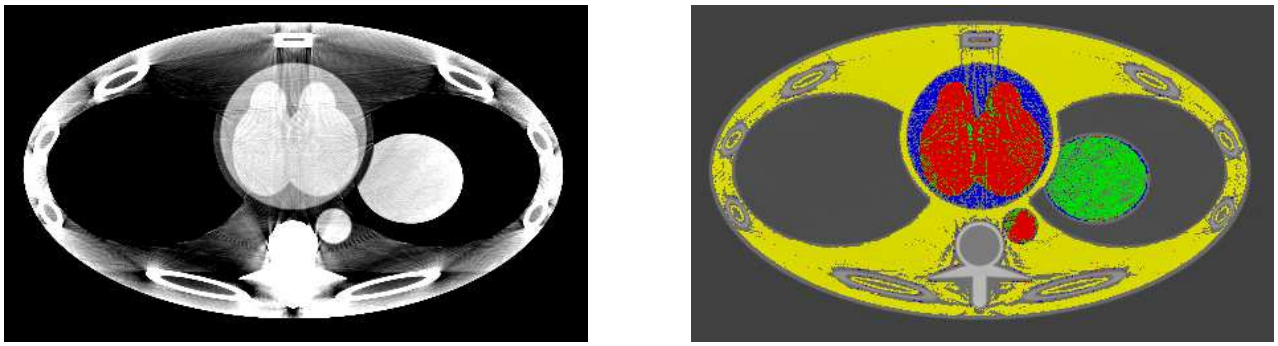

(a) (b)

Figure 6. (a) 80 kV input image (attuenuation values $\bar{\mu}(\mathbf{r})$, C: 0.220 mm^{-1}, W: 0.012 mm^{-1}); (b) Color-coded identification result. Blue: skeletal muscle, red: blood, green: liver, yellow: average soft tissue

3. CONCLUSION

The Local Spectral Reconstruction algorithm establishes a quantitative link between the CT measured weighted attenuation values and the spectral attenuation coefficient as the ground truth of the scanned object. We have

investigated possible applications in Quantitative CT such as quantitative beam-hardening corrections, energy calibrations and material decompositions. The convergence observed in the measured and simulated test cases is exponential and the accuracy has been found to be in the range of the CT measurement precision. However, a noise amplification takes place with increasing number of iterations. A good compromise between accuracy and precision is found for one to two LSR iterations. Finally, it was shown that the LWF result can be used to perform a direct material identification of dual-energy CT data. We conclude that the LSR algorithm can be applied to image-based spectral CT tasks with quantiative accuracy. Novel probabilistic material identification algorithms can be derived based on the LWF result.

REFERENCES

[1] B. Heismann and M. Balda, "Quantitative image-based spectral reconstruction for Computed Tomography," *Medical Physics*, under review.

[2] K. Taguchi, M. Zhang, E. C. Frey, J. Xu, W. P. Segars, and B. M. W. Tsui, "Image-domain material decomposition using photon-counting CT," J. Hsieh and M. J. Flynn, Eds., vol. 6510, no. 1. SPIE, 2007, p. 651008. [Online]. Available: http://link.aip.org/link/?PSI/6510/651008/1

[3] B. J. Heismann, J. Leppert, and K. Stierstorfer, "Density and atomic number measurements with spectral X-ray attenuation method," *Journal of Applied Physics*, vol. 94, no. 3, pp. 2074–2079, 2003.

[4] B. J. Heismann, K. Pham-Gia, W. Metzger, D. Niederloehner, and S. Wirth, "Signal transport in Computed Tomography detectors," *Nuclear Instruments and Methods in Physics Research Section A*, vol. 591, no. 1, pp. 28–33, 2008.

[5] "ICRU Report 46. Photon, Electron, Proton and Neutron Interaction Data for Body Tissues," *International Commission on Radiation Units and Measurements*, 1992.